Multi-material adhesively bonded structures: Characterisation and modelling of their rate-dependent performance

M. Lißner [a,*], B. Erice [b], E. Alabort [a,c], D. Thomson [a], H. Cui [d], C. Kaboglu [e], B.R.K. Blackman [e], M. Gude [f], N. Petrinic [a]

[a] *Department of Engineering Science, University of Oxford, Parks Road, Oxford, OX1 3PJ, United Kingdom*
[b] *Department of Structural Engineering, NTNU, Trondheim, 7491, Norway*
[c] *OxMet Technologies Ltd, Unit 15, Oxford Industrial Park, Yarnton, OX5 1QU, United Kingdom*
[d] *School of Aerospace, Transport and Manufacturing, Cranfield University, Bedford, MK43 0, AL, United Kingdom*
[e] *Department of Mechanical Engineering, Imperial College London, London, SW7 2, AZ, United Kingdom*
[f] *Institute of Lightweight Engineering and Polymer Technology (ILK), Technische Universitä,t Dresden, Dresden, 01307, Germany*

ABSTRACT

The rate-dependent failure response of multi-material adhesive joints for three deformation modes is investigated. A combination of carbon fibre reinforced polymers (CFRP) and titanium alloy Ti-6Al-4V is employed. The experiments provide important information about the failure sequence of a multi-material adhesive joints, which depends upon the loading rate regime. This is the first time that dynamic fracture mechanics experiments are performed in multi-material adhesive structures. The observed experimental results suggest a rate-dependent failure sequence for mode I dominated fracture. Simulations of the experiments are used to predict and rationalise the failure performance of the multi-material adhesive joint. The numerical analysis highlighted the importance of the individual knowledge of the rate-dependent mechanical performance of adhesive and composite to fully understand the fracture sequence of multi-material joints under impact.

1. Introduction and background

Lightweight design is a key technology in several industrial sectors such as the automotive and aerospace industry, where the decrease of mass is essential to reduce energy consumption and pollutant emissions [1]. For the electro-mobility, lightweight structures also play a crucial role to compensate for the heavy battery weight in hybrid and electric vehicles [2].

These lightweight structures can consist of dissimilar materials to take advantage of their individual material characteristics beneficial for the application. Traditionally, the materials are combined using joining methods such as welding, bolting or riveting. These require the materials to be thermally and/or chemically compatible to reduce stress concentrations and to be able to withstand the introduction of imperfections such as holes. Nevertheless, when using fibre reinforced polymers (FRP), adhesive joints are increasingly used [3]. The advantages of this joining technology are numerous: (i) avoidance of holes that introduce stress concentration; (ii) homogeneous stress distribution over a large area; (iii) avoidance of very high localised heating and associated heat affected zone of welded joints; and (iv) adhesive layers do not introduce significant additional weight.

However, the design of structural applications requires accurate failure prediction of the adhesively bonded joints. Several researchers have characterised the mechanical performance of multi-material combinations (particularly metal-to-composite) [4–10]. On one hand, some of these investigations reported the influence of adherent combinations on the joint strength [11–16] while on the other hand, others examined the fracture energy, J, for multi-material combinations [17–24]. Some researchers studied the bond behaviour as a function of the adherent material properties and their combination with brittle and ductile adhesives [8,25]. Others considered multi-material adhesive joints targeting specific applications such as marine applications or bus structures [7, 26]. Most of these relied upon quasi-static experimentation to measure strength and fracture energy. However, many applications where weight reduction is critical are likely to be subjected to various loading regimes such as crashworthiness in automotive structures, and hail or bird strike impacts on aerospace structures [27]. To the authors best knowledge, there are only a few investigations which aim to understand the mechanical behaviour of multi-material adhesive joints under those conditions [9,28–30]. These studies relied upon the use of single lap joint (SLJ) and double lap joint (DLJ) experiments to measure
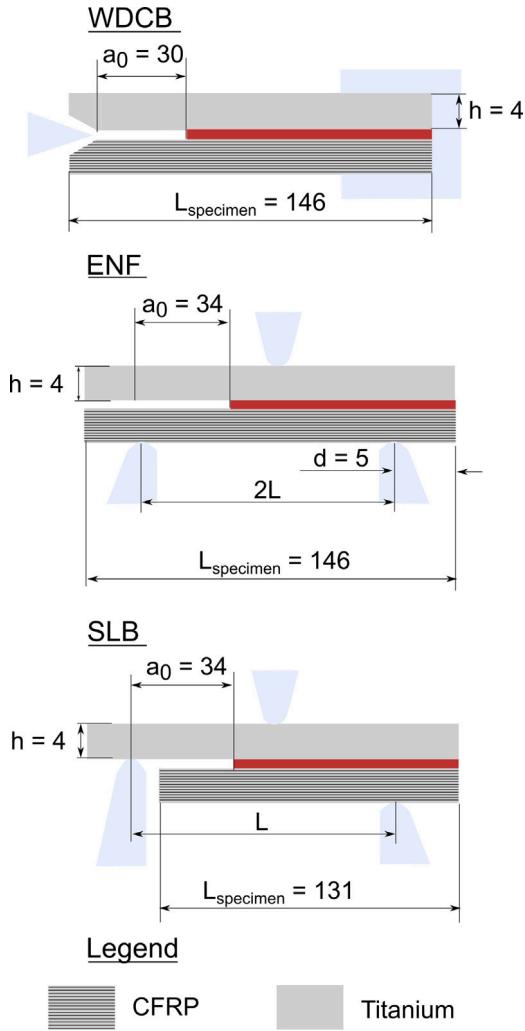
Fig. 1. Specimen dimensions for each fracture mode configuration in [mm].

Fig. 2. Demonstration of the (a) used bonding fixture to manufacture the specimens and (b) the adhesive thickness qualification for each fracture mode individually.

the performance under dynamic loading regimes. Although, adhesive joints are normally designed to exhibit advantageous shear loading behaviour (mode II), their performance in normal loading (mode I) remains critical. Moreover, both the bond strength and the fracture energy can exhibit rate-dependent behaviour — this has been observed both in metal-to-metal [27,31–35] and composite-to-composite [36–39] adhesive joints.

Therefore, in order to understand the mechanical performance of multi-material adhesive joints, it is necessary to investigate their behaviour under different fracture modes and loading rates. This is the main focus of the present work. Multi-material adhesive joints between carbon fibre reinforced plastic (CFRP) composites and titanium alloy have been investigated. Firstly, fracture mechanics experiments in the form of wedge double cantilever beam (WDCB), end notched flexure (ENF), and single leg bending (SLB) specimens were performed both quasi-statically and dynamically. Secondly, microscopy analysis was carried out to identify the fracture mechanisms for each fracture mode. Thirdly, experimental results for similar and multi-material combinations (titanium-to-titanium and CFRP-to-titanium) have been compared in order to quantify the influence of the adherent material. Fourthly, simulations of the experiments have been performed using a material model developed for the adhesive layer. Finally, the experimental results have been used to assess the ability of the model to predict the failure phenomena of adhesively bonded structures with multi-materials in a rate and fracture mode dependent manner.
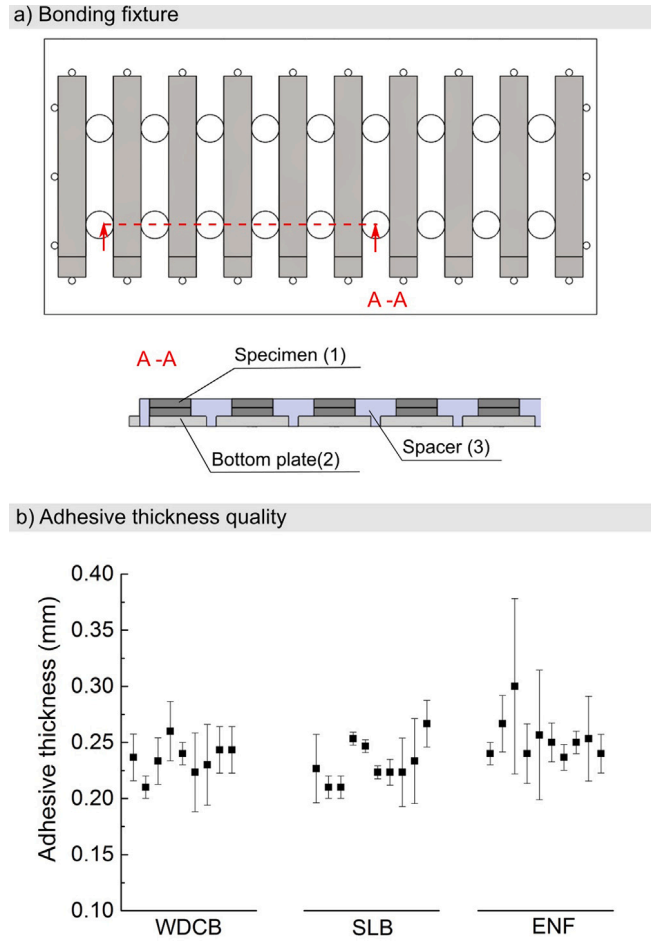
2. Experimental methods

This section provides detailed information on the used materials. Also, the experimental setup for performing rate-dependent investigations is explained. Then, a special data acquisition method developed for dynamic fracture mechanics experiments is described [34]. Finally, the high-resolution method employed to analyse the fracture mechanisms is explained.

2.1. Adherent and adhesive material

The multi-material adhesive joints were adhesively bonded using the thermosetting epoxy resin AF 163-2OST from Scotch-Weld™. AF 163-2OST is supported with a glass fibre carrier matt to enable the handling of the film adhesive when bonding large structures. The abbreviation OST stands for one side tacky with non-woven carrier (matt) on low tack surface. The as received composite panels were made out of the CFRP IM7/8552 material system prepregs. The titanium parts were made out of the titanium alloy Ti–6Al–4V. The characteristics for each adherent material are listed in Tables 1 and 2. The listed K and H parameters in Table 1 denote the arbitrary parameters of the fitting function developed by Hoffmann [40] to consider the rate-dependent behaviour. This functions is shown as follows

$$\kappa = 1 + (K\dot{\varepsilon})^{\frac{1}{H}} \tag{1}$$

where κ represents the scale factor for the relevant material properties of the composite and $\dot{\varepsilon}$ is the strain-rate associated with the appropriate deformation mode.
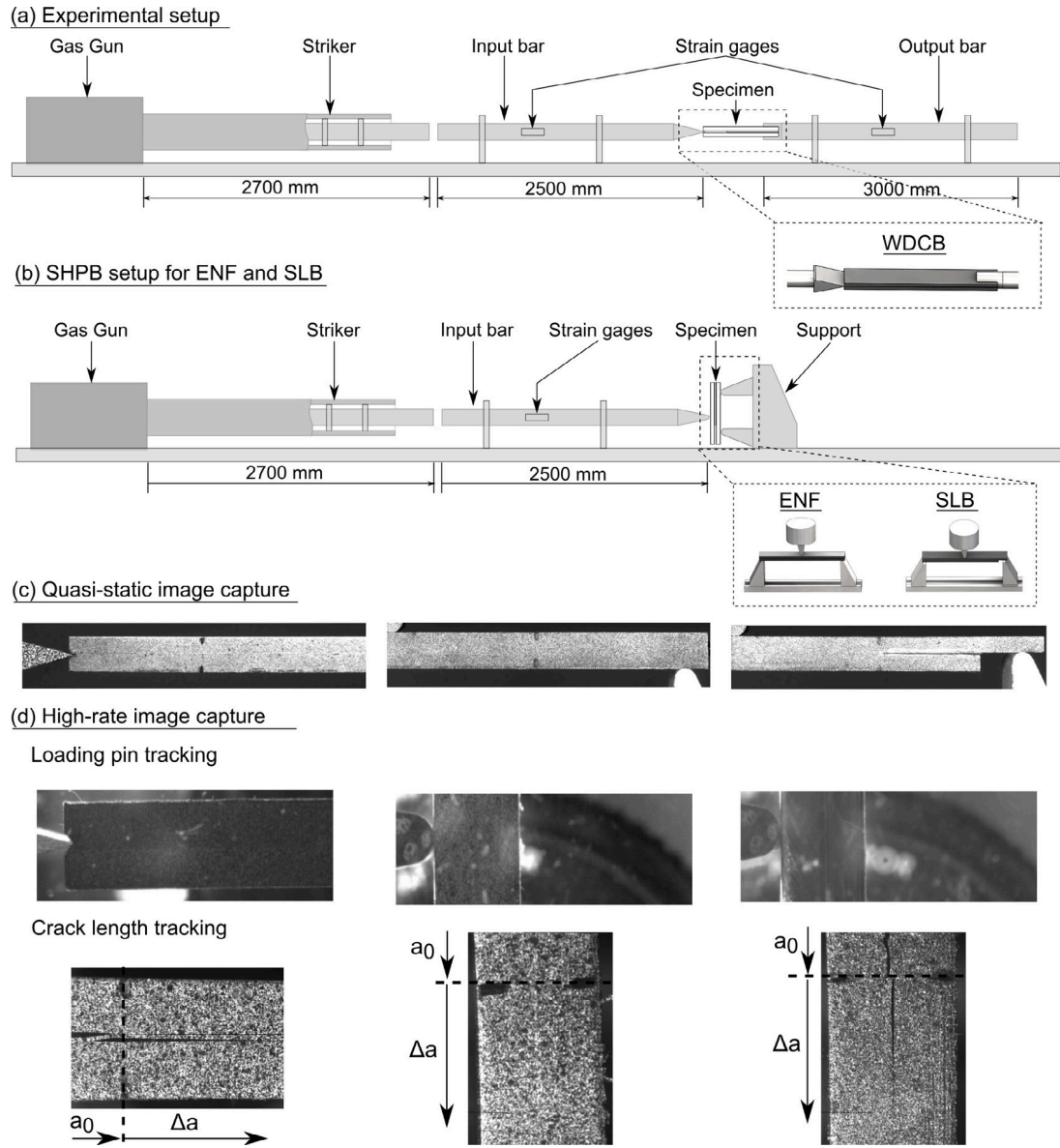
Fig. 3. Graphical demonstration of (a) the experimental setup, (b) the quasi-static image capturing and (c) the image tracking of loading pin and crack length for high-rate loadings.

Table 1
Material properties of adherents, bars, striker, and supports, [41].

Metal	E (GPa)	ρ (g/cm^3)	ν	σ_y (MPa)
Ti–6Al–4V	114	4.43	0.34	900
Steel	200	8	0.29	–

Table 2
Material properties of the composite IM7/8552, [40].

	QS	K	H
E_{11}	162000 MPa	–	–
E_{22}	9400 MPa	$6.62E^{-6}$	4.73
E_{33}	9400 MPa	$6.62E^{-6}$	4.73
G_{12}	4634 MPa	$8.33E^{-4}$	2.29
G_{13}	4634 MPa	$8.33E^{-4}$	2.29
G_{23}	5600 MPa	–	–
ν_{12}	0.316	–	–
ν_{13}	0.316	–	–
ν_{23}	0.5	–	–

The specimens were designed to investigate the failure performance of three different fracture modes: the wedge double cantilever beam (WDCB), the end notched flexure (ENF) and the single leg beam (SLB) specimen. The WDCB specimens were used to investigate the failure performance of the joint under normal loading in mode I. The shear behaviour (mode II) was investigated by the use of ENF specimens. A combination of both loading modes was investigated when employing the SLB specimens. Fig. 1 shows the specimen dimensions for each fracture mode. From an application perspective, the composite is reinforced with titanium through adhesive bonding. The specimens were loaded such that the metallic adherent deforms first, followed by the composite adherent. A reversed order is believed to result in a damage of the

composite part, which may prevent the damage of adhesive bonding, which is out of the scope of the paper.

2.2. Carbon fibre reinforced plastic layup

The purpose of the performed fracture mechanics experiments is to provide an extra set of experimental data to validate a cohesive zone
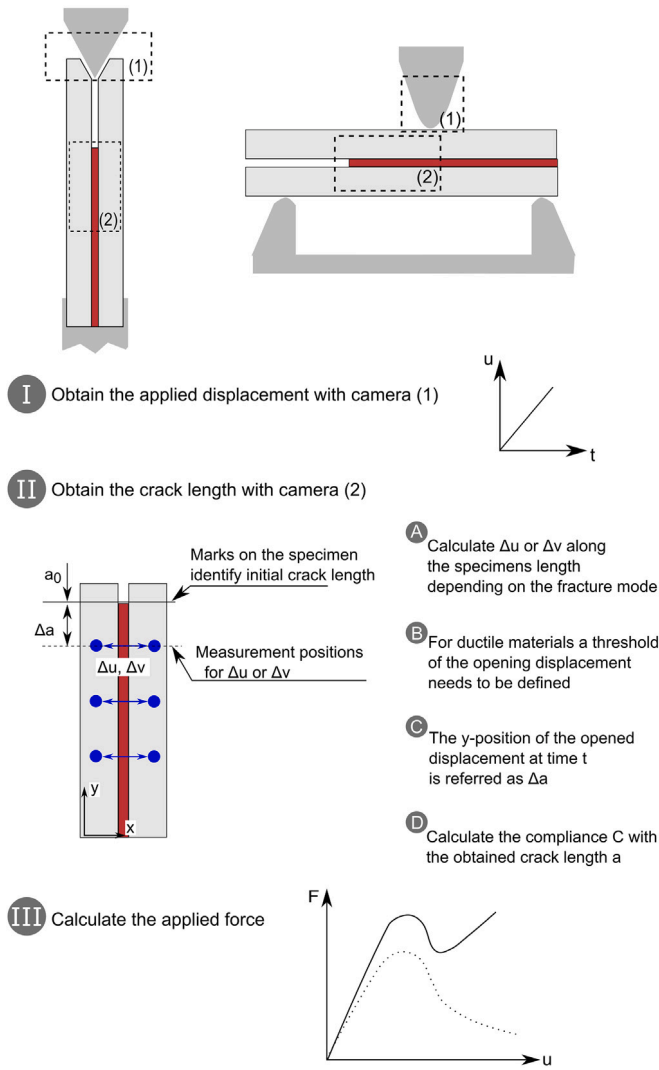
Fig. 4. Graphical illustration of the data acquisition method used to obtain the force–displacement behaviour of dynamic fracture mechanics experiments.

model for the adhesive layer, previously developed by the authors [33], and to understand the failure performance of multi-material adhesive joints. Therefore, the experiments were designed to obtain mode I, mode II and mixed-mode fracture within the adhesive layer. Hence, the composite part in this investigation was designed to have a similar flexure rigidity (EI) to the titanium part. This was achieved by designing the ply layup accordingly: In the ABD matrix for quasi-isotropic layups, the parameter D_{11} represents the bending stiffness which is here compared to the bending stiffness of the titanium part calculated with

$$D_{11} = EI \tag{2}$$

where E is the Young's modulus of the titanium and I is the second moment of inertia. The length, width and adherent thickness are the same for both material parts. Hence, the flexure rigidity of the composite is $D_{11} = 604393.54$ MPa for a ply layup of $[45/-45/0/0/45/0/0/0/0/0/-45/0/45/0/-45/0/-45/0]_s$. Thus, the 45° ply angle is in contact with the adhesive. As a comparison, the bending stiffness of the titanium part is 608000 MPa. The authors are aware of the difficulty to achieve the exact same bending stiffness of both multi-material adherents. However, since these fracture mechanics experiments are not used to characterise the fracture energy of the adhesive layer, the suggested specimen configurations (WDCB, ENF, SLB) are considered.
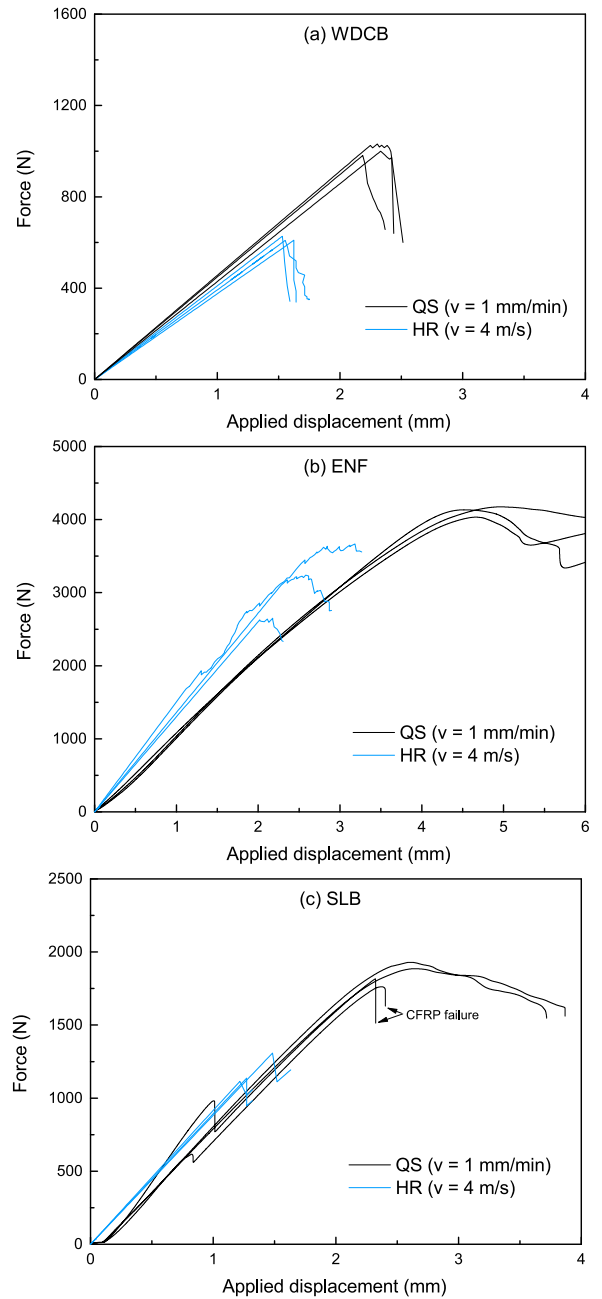

Fig. 5. Rate-dependent experimental results of CFRP-titanium adhesive joints for: (a) WDCB, (b) ENF, and (c) SLB.

2.3. Specimen manufacture and materials

To accurately manufacture the specimens, a custom made bonding fixture was designed — see Fig. 2(a). To apply the correct adhesive thickness, spacers were employed. They had a thickness of 8.3 mm to account for the ideal total thickness of the adhesive joint. The individual measurements of the as received titanium and CFRP parts revealed in a nominal thickness of 3.80 and 4.25 mm respectively. Preparation of the surfaces of the adherents is required to improve the bond quality. For the titanium parts, the surfaces were grit-blasted, cleaned, etched and anodised following a procedure described elsewhere [42]. The composite parts were grit-blasted and then wiped clean with an acetone soaked, lint free cloth. To introduce the initial crack length, a 12.0 μm thick Teflon sheet was inserted between two layers of film adhesive. Afterwards, the specimens were cured for 1 h at 121 °
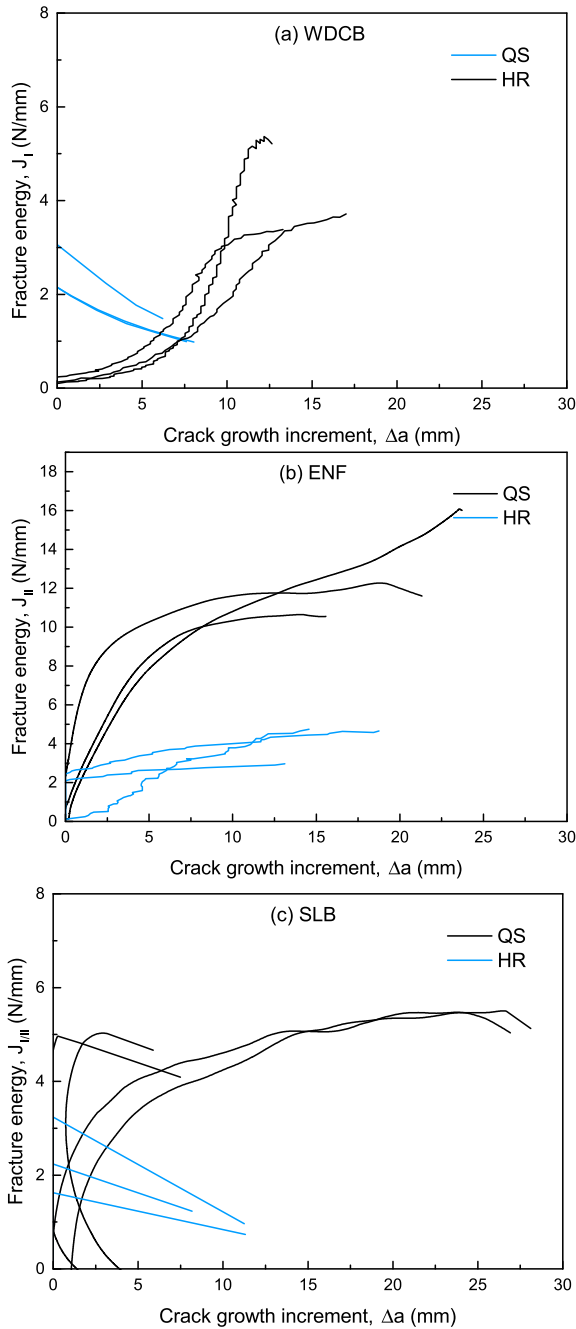
Fig. 6. Rate-dependent experimental results of the CFRP-titanium fracture energy for:(a) WDCB, (b) ENF, and (c) SLB.

C under a pressure of 1.4 bar. The measured adhesive layer thickness of the manufactured specimens is reported for each fracture mode in Fig. 2(b). A deviation of 5.96%, 8.00% and 7.40% for the WDCB , ENF and SLB from the nominal adhesive thickness of $t_a = 0.25$ mm was observed.

2.4. Experimental setup: QS and HR fracture mechanics experiments

The quasi-static (QS) and high-rate (HR) experiments were performed in laboratory conditions to obtain three repeatable test results. A screw-driven Zwick machine was employed to load the specimens quasi-statically with a constant cross-head speed of $v = 0.016$ mm/s.

The load–displacement ($F - u$) curve was recorded during the experiment. A prism-based line Jai camera recorded images of the tested specimen at 2 frames per second and a resolution of 1550 x 2150 pixels. A fine grey-scale speckle pattern was applied to the surface of the specimen to monitor the crack length advancement Δa using digital image correlation (DIC). The initial crack length a_0 was marked with a ruler as it is shown in Fig. 3. The HR experiments were carried out using a Split Hopkinson Pressure Bar (SHPB) to subject the specimen to a velocity of $v = 4000$ mm/s [34]. Images were recorded using two high-speed cameras: a Photron SA-5 camera recorded the displacement of the loading wedge/pin at 150,000 frames per second with a resolution of 716 x 624 pixels while a Specialised Imaging Kirana camera monitored the crack length growth at 200,000 frames per second with a resolution of 9244 x 768 pixels. Fig. 3 shows the QS and HR setup for each fracture mode respectively.

2.5. Data acquisition and analysis procedure

The quasi-static (QS) force–displacement curves for ENF and SLB experiments can be measured directly from the testing machine and DIC output. However, for QS WDCB experiments and for all high-rate (HR) experiments, the force and displacement measurements were obtained from DIC because the measured load values are influenced by friction between wedge and adherent as well as the often unreliable force readings using strain gauges in the SHPB [34]. Therefore, grey scale recordings from one-camera system for the QS and two-camera systems for HR experiments were used to determine both the applied displacement and the crack length. The crack length enables the calculation of the compliance using relevant equations based on the beam theory for the different fracture modes which is explained below. This step is followed by the relationship between displacement u and compliance C to obtain the force F following

$$F(u) = \frac{u}{C} \quad . \tag{3}$$

Fig. 4 explains schematically this measurement method. Detailed information about this method and its relevant equations and approaches can be found in previous work from the authors [34].

The calculation of the compliance follows different equations for the different fracture modes and is based on the simple beam theory and the Timoshenko beam theory — to account for shear effects. For the WDCB experiments, the compliance is obtained following [43]

$$C(a) = \frac{8a^3}{Ebh^3} + \frac{12a}{5bhG} \tag{4}$$

where a is the crack length, b is the specimen width, h is the beam height, E is the Young's modulus and G is the shear modulus of the adherent. This equation is only suitable when the two dissimilar beams deform equally or with insignificant variations. Otherwise, the reader is referred to Wang et al. [10].

The compliance for ENF [43] and SLB [44] experiments are estimated following

$$C(a) = \frac{3a^3 + 2L^3}{8bh^3 E} + \frac{3L}{10bhG} \tag{5}$$

and

$$C(a) = \frac{28a^3 + L^3}{32Ebh^3} + \frac{3(a + L)}{20Gbh} \tag{6}$$

respectively, where L is half the distance between the supports for the ENF specimens and L is the whole distance between the supports for the SLB specimens.

Table 3 summarises all required equations in order to obtain the force–displacement readings for QS and HR WDCB, ENF and SLB experiments. Detailed information about equations and approaches are given in the relevant references. For subsequent comparison, equations for calculating the fracture energy of each specimen configuration are also given in Table 3.

(a) Immediate crack propagation into composite adherent
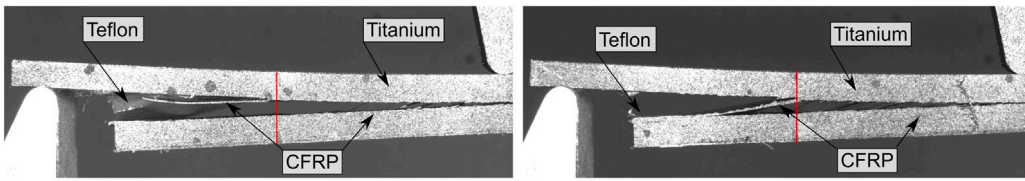
(b) Crack propagation first through adhesive layer and then migration into composite adherent
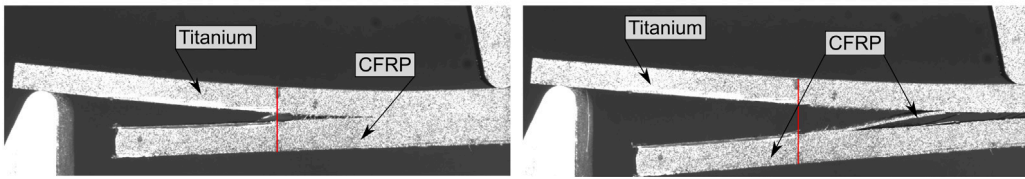

Fig. 7. Observed crack path for quasi-static SLB specimens for (a) immediate crack propagation into the composite adherent and (b) desired crack propagation within adhesive layer. The red line highlights the initial crack.
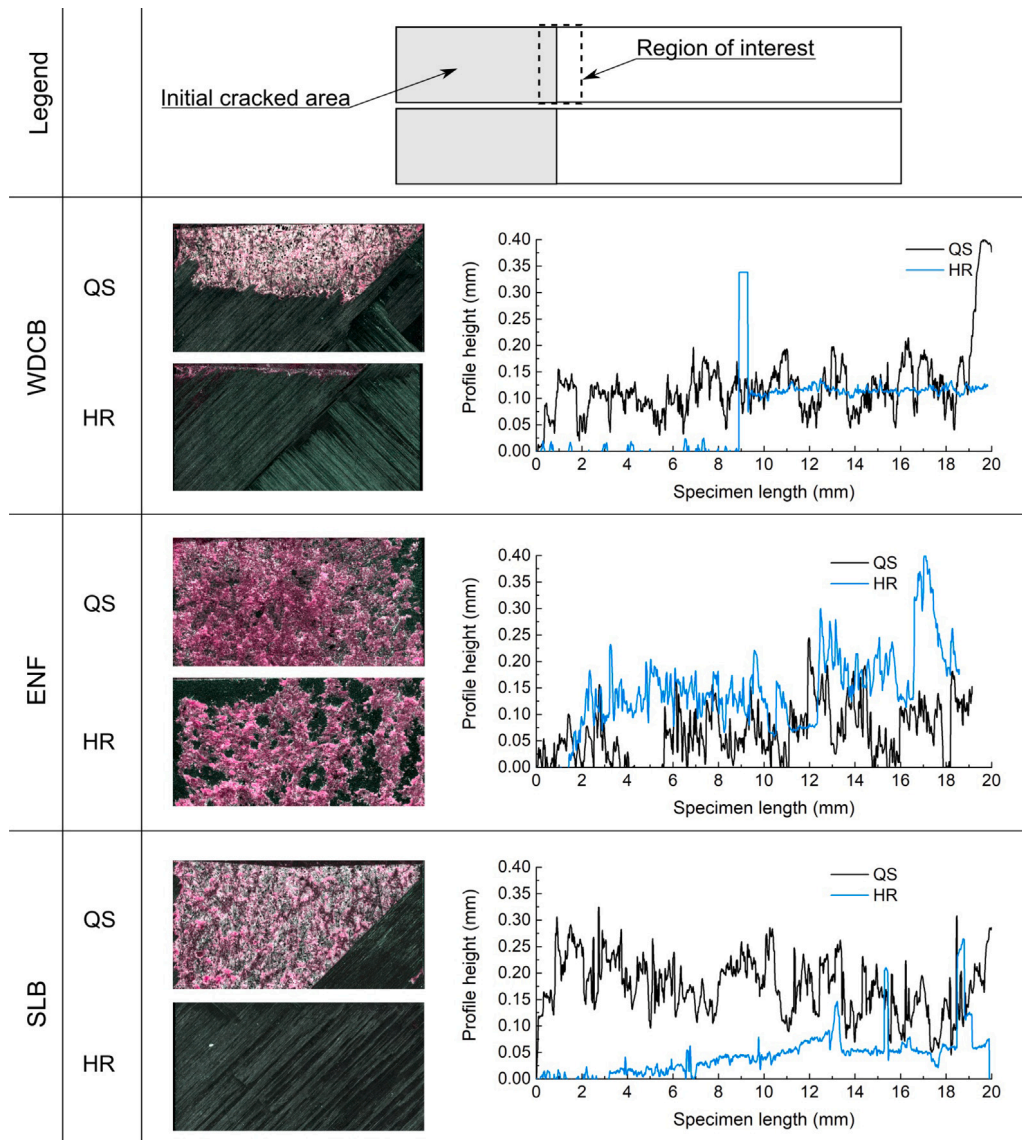

Fig. 8. Profile height of representative fractured surfaces for the investigated fracture mechanics experiments.

As a remark, the performed fracture mechanics experiments are used to understand the failure performance of a multi-material adhesive joint in different loading rate regimes. This work's aim is to investigate the rate-dependent failure performance of multi-material adhesive
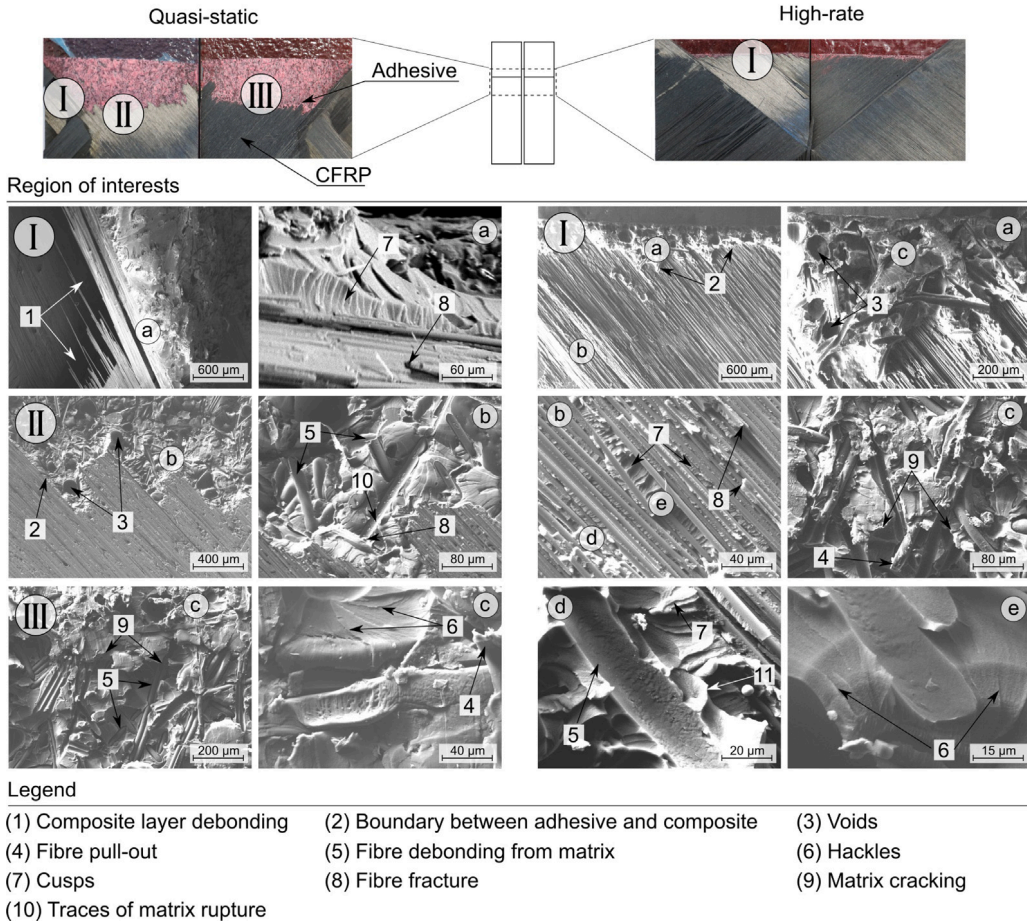
Wedge double cantilever beam (WDCB) experiments

Region of interests

Legend

(1) Composite layer debonding
(2) Boundary between adhesive and composite
(3) Voids
(4) Fibre pull-out
(5) Fibre debonding from matrix
(6) Hackles
(7) Cusps
(8) Fibre fracture
(9) Matrix cracking
(10) Traces of matrix rupture

Fig. 9. Micrographs of the failure surface of WDCB experiments under quasi-static (left) and high-rate (right) loading rates.
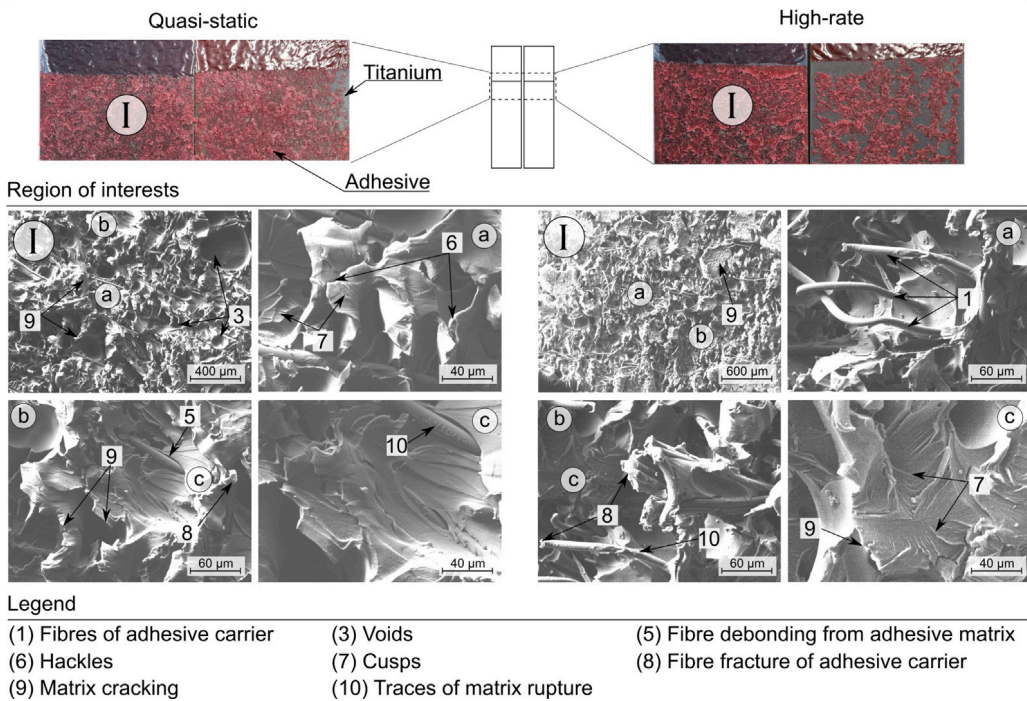
End notched flexure (ENF) experiments

Region of interests

Legend

(1) Fibres of adhesive carrier
(3) Voids
(5) Fibre debonding from adhesive matrix
(6) Hackles
(7) Cusps
(8) Fibre fracture of adhesive carrier
(9) Matrix cracking
(10) Traces of matrix rupture

Fig. 10. Micrographs of the failure surface of ENF experiments under quasi-static (left) and high-rate (right) loading rates.
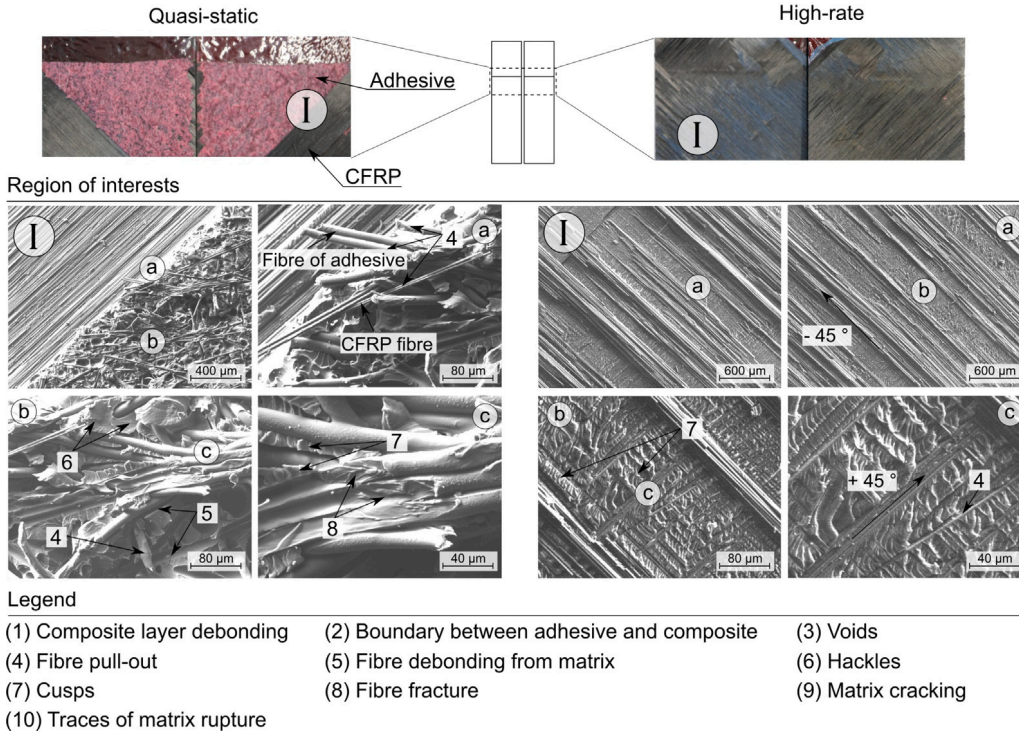
Single leg beam (SLB) experiments

Quasi-static

High-rate

Adhesive

CFRP

Region of interests

Legend

(1) Composite layer debonding
(2) Boundary between adhesive and composite
(3) Voids
(4) Fibre pull-out
(5) Fibre debonding from matrix
(6) Hackles
(7) Cusps
(8) Fibre fracture
(9) Matrix cracking
(10) Traces of matrix rupture

Fig. 11. Micrographs of the failure surface of SLB experiments under quasi-static (left) and high-rate (right) loading rates.

joints — and their sequence of failure. For the characterisation of the fracture energy, the reader is referred to previous publications of the authors [33,34]. Therefore, the above-mentioned equations are used for a simplified analysis of the mechanical response of the adhesive joints.

2.6. Microstructural and fractography analysis

The analysis of the fractured surface was carried out to investigate the existence of cohesive failure within the adhesive layer and to understand the failure phenomena of the composite and the adhesive layer. For that, a 3D optical microscope (Alicona) was used to measure the profile height of the fractured surfaces. Then, the specimens were prepared for metallographic studies. The surfaces were gold-coated in order to make the surfaces conductive for post-mortem SEM analysis. Measurements were taken using a Zeiss EVO scanning electron microscope (SEM) to investigate the failure mechanisms for each material independently.

3. Results and discussion

Experiments were performed at two different loading rates in the three different fracture mode configurations. Microscopy analyses of the fractured surfaces were used to investigate the fracture processes. By comparing the current results with experiments of titanium-to-titanium alloy adhesive joints [34], the influence of the adherent material has been quantified.

3.1. On the rate dependent behaviour of fracture mechanics experiments

Experiments for three different fracture mode configurations (WDCB, ENF, SLB) were performed under laboratory conditions. The force–displacement curves were obtained using the data acquisition method described in Section 2.5 and Lißner et al. [34].

Fig. 5 shows the experimental force–displacement curves for each tested condition. The compliance for the two beams of the WDCB
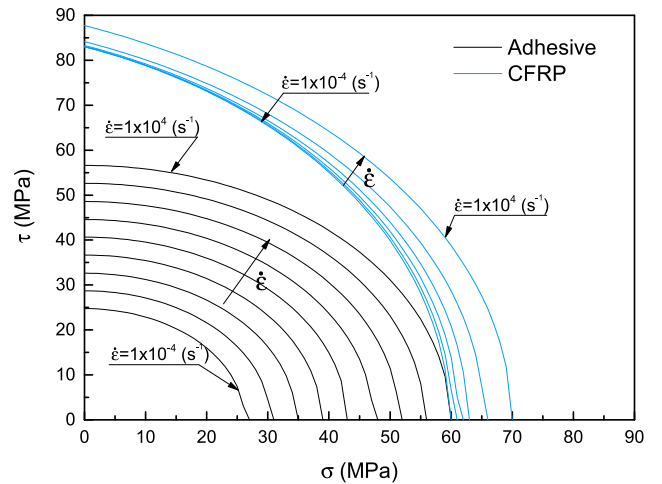

Fig. 12. Shear-Normal behaviour representation of the rate-dependent failure envelope for the CFRP and the adhesive layer individually.

experiments was obtained individually to investigate whether there is a significant difference in value. For the titanium, the compliance is 0.0011 mm/N, while for the composite it is 8.2 x 10^{-4} mm/N. The difference between both compliance values amounts to 2.9 x 10^{-4} mm/N. Analytical analysis suggests that this will induce small deviations: this difference revealed in an energy and force influence of 3% and 6% respectively. Therefore, the analysis is performed assuming equal deformation of the two different beams.

For the QS loading rate regime, the maximum force for WDCB experiments was 1001 ± 24.5 N, while for ENF experiments the maximum force was $F = 4116.8 \pm 47.9$ N. The maximum force for SLB experiments was $F = 1905.7 \pm 31.3$ N. The experiments in HR loading rate regime exhibit a maximum force of $F = 613.2 \pm 12.2$ N, $F =$

Table 3

Overview of the employed equations for the calculation of the fracture energy in QS and HR loading regimes,[34].

Equations for analysis	Wedge double cantilever beam (WDCB)	End notched flexure (ENF)	Single leg beam (SLB)
Compliance	$C(a) = \frac{8a^3}{Ebh^3} + \frac{12a}{5bhG}$	$C(a) = \frac{3a^3+2L^3}{8bh^3 E} + \frac{3L}{10bhG}$ $C_c = C - \frac{3L}{10bhG}$ and $C_{0c} = C_0 - \frac{3L}{10bhG}$	$C = \frac{F}{u}$
Energy release rate	$J_{Ic}(a, F) = \frac{12a^2}{Eh^3b^2} F^2 + \frac{F}{b}(w_1' - w_2')$ $w_1' - w_2'$ have been calculated following the procedure described in [45]	$J_{IIc}(a_e, F) = \frac{9F^2 a_e^2}{16b^2h^3 E_f}$ with $E_f = \frac{3a_0^3+2L^3}{8bh^3}\left(C_0 - \frac{3L}{10bhG}\right)^{-1}$	$J_{I/IIc}(a, F) = \frac{21F^2 a^2}{16 E_f b^2 h^3} + \frac{3F^2}{10Gb^2 h}$ $J_{Ic}(a, F) = \frac{12F^2 a^2}{16 E_f b^2 h^3} + \frac{3F^2}{10Gb^2 h}$ $J_{IIc}(a, F) = \frac{9F^2 a^2}{16 E_f b^2 h^3}$ with $E_f = \frac{28a_0^3+L^3}{32bh^3}\left(C_0 - \frac{3(a_0+L)}{20bhG}\right)^{-1}$
Quasi-static			
Crack length	Obtained with new measuring technique based on DIC using high-speed SI Kirana camera images	$a_e = \left[\frac{C_c}{C_{0c}} a_0^3 + \frac{2}{3}\left(\frac{C_c}{C_{0c}}-1\right)L^3\right]^{\frac{1}{3}}$	Transform cubic equation to obtain the crack length a $C(a) = \frac{28a^3+L^3}{32Ebh^3} + \frac{3(a+L)}{20Gbh}$
Displacement		DIC or testing machine output	
Force	$F(u) = \frac{u}{C}$		Testing machine output
High-rate			
Crack length	Obtained with new measuring technique based on DIC using high-speed SI Kirana camera images		
Displacement	Obtained with DIC using high-speed Photron camera images		
Force	$F(u) = \frac{u}{C}$		

Table 4

Fracture energy for WDCB, SLB and ENF experiments using CFRP-TI material combination.

	WDCB	SLB	ENF
QS	4.54 ± 1.04 N/mm	4.05 ± 0.35 N/mm	10.75 ± 0.48 N/mm
HR	2.26 ± 0.21 N/mm	1.90 ± 0.06 N/mm	3.03 ± 0.81 N/mm

3150.8 ± 496.6 N and $F = 1183.4 \pm 103.1$ N for WDCB, ENF and SLB specimens respectively. For all tested fracture mode configurations, the force decreases with increasing loading rate. This is believed to be caused by the decrease of fracture energy of the adhesive with increasing loading rate. The calculated fracture energy shown in Table 4 and Fig. 6 for each fracture mode configuration provide evidence for this. Similar results were found by Lißner et al. [33,34].

Two of the QS SLB experiments failed before reaching the maximum force and before exhibiting ductile behaviour — see Fig. 5(c). Fig. 7(a) shows the corresponding specimens with delamination failure of the CFRP part which explains the sudden drop in force. The excess adhesive in these first two tests might have caused the immediate crack propagation into the composite due to a local higher transverse stress state. Similar effects have been observed by Blackman et al. [46] who related the unstable crack growth to the higher transverse tensile stress generated in the mixed-mode specimens. In comparison, the remaining QS SLB specimens showed a crack propagation within the adhesive layer up to a certain point at which the transverse stress of the composite was reached — see Fig. 7(b). This caused the crack to migrate into the composite. Fig. 5(c) supports this statement as an unstable crack propagation can be observed.

3.2. Analysis of the fracture observations

The fracture surface was investigated to identify the mechanisms of failure. Firstly, it is important to identify when cohesive fracture within the adhesive layer occurs so that one can confidently relate the measured force–displacement behaviour and the calculated fracture energy to the adhesive layer. Three-dimensional optical microscopy was applied to measure the profile height of the fractured samples. Fig. 8 shows the profile height for each fracture mode and loading condition. In the QS experiments, the adhesive layer fractured in a cohesive manner: this is supported by the average measured profile height of 0.14 mm. This is observed independently of the fracture modes. However, in HR, only ENF experiments show cohesive failure

of the adhesive layer. WDCB and SLB experiments experienced failure within the CFRP.

Figs. 9, 10, and 11 show SEM images of the fractured samples for WDCB, ENF and SLB respectively. The following features are observed in all QS samples (numbers correlate with the areas highlighted in Figs. 9, 10, and 11): voids (3), fibre pull-out (4), fibre debonding from the matrix (5), hackles (6), cusps (7), fibre fracture (8), matrix cracking (9) and traces of matrix rupture (10). Typical shear behaviour phenomena such as hackles (6) and cusps (7) are more pronounced for ENF specimens — see Fig. 10.

Micrographs for QS conditions presented in Fig. 9 show that WDCB specimens exhibit a change of fracture mode between the adhesive and the CFRP — see area (2) in Fig. 9. This boundary area suggests an initial crack propagation through the adhesive until a certain applied transverse tensile stress of the composite matrix is reached. This enabled the crack to propagate into the composite, leading to delamination of the full part — see Fig. 9. Similar crack propagation phenomena is observed in QS SLB — see the analogous micrographs presented in Fig. 11. On the other hand, micrographs in Fig. 10 show that QS ENF experiments failed completely in a cohesive manner of the adhesive layer.

In HR, only ENF experiments show a failure of the adhesive layer. The length of cusps (7) lines suggests a difference in mechanism as a function of the loading rate: the cusps lines in QS appear to be longer than in HR. This behaviour can be related to the decrease of energy necessary to separate the two surfaces with increasing loading rate. In HR WDCB, crack initiation was in the adhesive, but the crack immediately propagated into the composite adherent leading to an interlaminar failure path. HR SLB samples show complete fracture by delamination of the CFRP — see Fig. 11.

3.3. Comparison of the fracture properties of adhesive and CFRP

The different failure sequence of the adhesive joint in QS and HR loadings can be explained by comparing the individual rate-dependent fracture behaviour of the CFRP and the adhesive. A failure envelope of the strength for both materials is presented in Fig. 12, where the CFRP's envelope is based on Puck's failure theory. The inter fibre failure (IFF) criterion for the 2D analysis is summarised in the following

$$f_{E,IFFA} = \sqrt{\left(\frac{\tau}{R_{\perp\parallel}}\right)^2 + \left(1 - p_{\perp\parallel}^{(+)}\frac{R_\perp^{(+)}}{R_{\perp\parallel}}\right)^2 \left(\frac{\sigma_2}{R_\perp^{(+)}}\right)^2} + p_{\perp\parallel}^{(+)}\frac{\sigma_2}{R_{\perp\parallel}} \quad for\ \sigma > 0$$
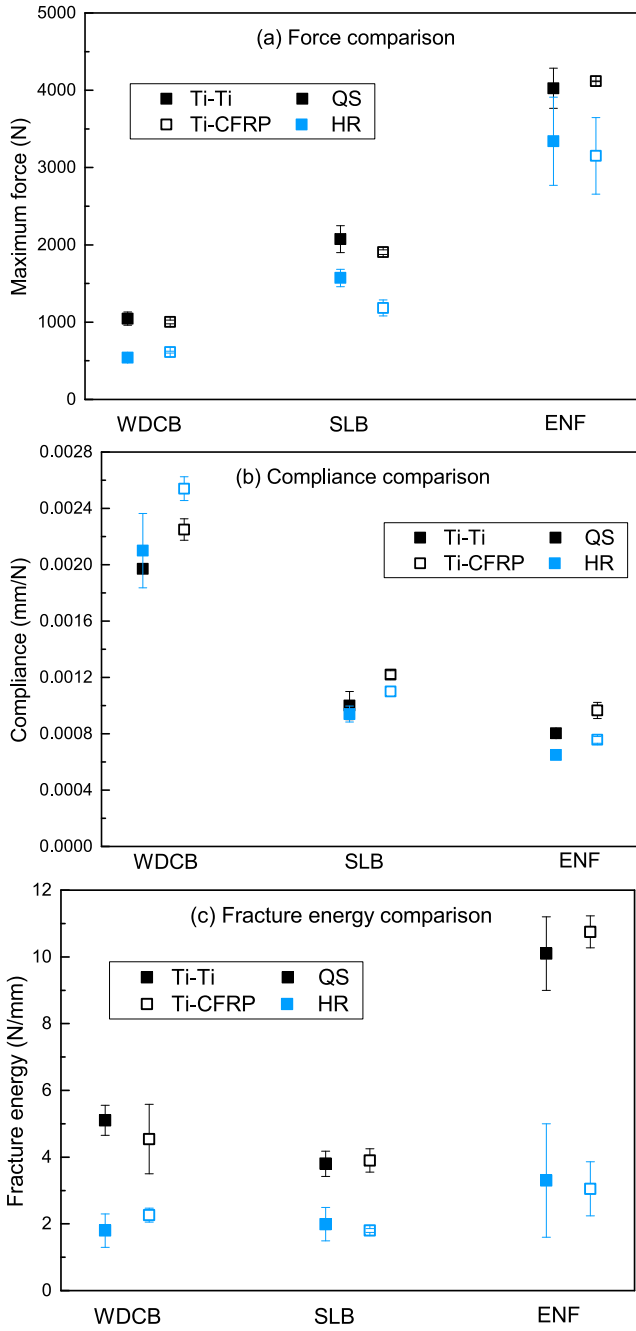
(7)

Fig. 13. Comparison of the quasi-static and high-rate (a) maximum force, (b) compliance and (c) fracture energy of similar (Ti-Ti) and multi-material (CFRP-TI) adhesive joints for (a) WDCB, (b) SLB and (c) ENF.

where the reader is referred to Puck and Schürmann [47] for the detailed explanation of all parameters. The failure envelope for the adhesive was generated using the quadratic stress criterion following the equation

$$\left(\frac{t_{\mathrm{m1,I}}}{T_{\mathrm{N}}}\right)^2 + \left(\frac{t_{\mathrm{m1,II}}}{T_{\mathrm{S}}}\right)^2 = 1 \ , \tag{8}$$

where $t_{\mathrm{m1,I}}$ and $t_{\mathrm{m1,II}}$ are the yield stress components, and T_{N} and T_{S} are the maximum traction components for mode I and II, respectively [33].

The individual rate-dependent properties are provided in Lißner et al. [33],Hoffmann [40] for the adhesive and the CFRP respectively. The shear and normal stresses for the CFRP are represented by the equivalent stresses in normal and shear direction. It is shown that the

adhesive indicates a more pronounced rate-dependency than the CFRP. Additionally, due to the difference in thickness of the components (adhesive and CFRP plate), the adhesive experiences a substantially higher strain rate than the CFRP. This means that under dynamic loading conditions, the adhesive and the CFRP have a similar fracture stress — see Fig. 12. This is supported by our fracture observations: see for example the thin fractured adhesive line in HR WDCB which is shown in Fig. 9. Consequently, the knowledge of the individual rate-dependent behaviour of CFRP and adhesive is of utmost importance for understanding the failure sequence of multi-material adhesive joints — this is discussed next.

3.4. Comparison of Ti-Ti and CFRP-Ti material combinations in fracture mechanics experiments

In order to better understand the influence of the adherent materials on the mechanical performance of the adhesive joint, experimental results of similar [34] and multi-material (CFRP-Ti) combinations are compared. The failure mode of Ti-Ti adhesive joints was cohesive failure of the adhesive layer for all investigated fracture mode configurations (WDCB, ENF and SLB), Lißner et al. [34]. The results of this comparison are presented in Fig. 13 for QS (black) and HR (blue) loading regimes.

For QS conditions, Fig. 13(a) shows that the average maximum forces for each fracture mode are similar for both Ti-Ti and CFRP-Ti material combinations. Fig. 13(b) shows that the stiffness of the multi-material combination appears to be slightly lower than the similar material combination: CFRP-Ti shows a larger compliance — which is the inverse of the stiffness. Although, the ply layup of the CFRP was designed to match the flexure rigidity of the titanium, the bending stiffness is approximately 3607 MPa lower. This difference in flexure rigidity can explain the lower stiffness of the CFRP.

However, in HR, only WDCB and ENF experiments suggest similar failure behaviour between Ti-Ti and CFRP-Ti material combinations. This is evidenced in the force and in the fracture energy comparison graphs shown in Fig. 13(a) and 13(c) respectively. In contrast, HR SLB experiments with a multi-material combination showed CFRP fracture (see Fig. 11) instead of failure within the adhesive layer. This is validated by the lower force and fracture energy of the CFRP-Ti combination when compared to Ti-Ti fracture experiments. The minor deviation of the force and fracture energy of HR SLB experiments for both material combinations suggests that the failure stress of adhesive and CFRP have been similar in the SLB experiments — as suggested in Fig. 12. Moreover, it is believed that the failure path occurred since the transverse stress of the composite has been exceeded. Opposed to the QS mechanical performance – where the adhesive layer is the weakest link independently of the adherent material of choice – HR experiments reveal a dependency of the adherent material on the failure sequence.

4. Numerical modelling of multi-material adhesively bonded structures

Simulations of the experiments were carried out to investigate the ability of a cohesive zone model to simulate the failure process of a multi-material adhesive joint. This CZM was previously developed and validated by the authors [33,34]. This section summarises the model of the adhesive layer and provides information about the finite element setup for the fracture mechanics experiments for WDCB, ENF, and SLB specimens. Fig. 14 illustrates the method which has been followed in order to achieve a reliable prediction of the failure performance.
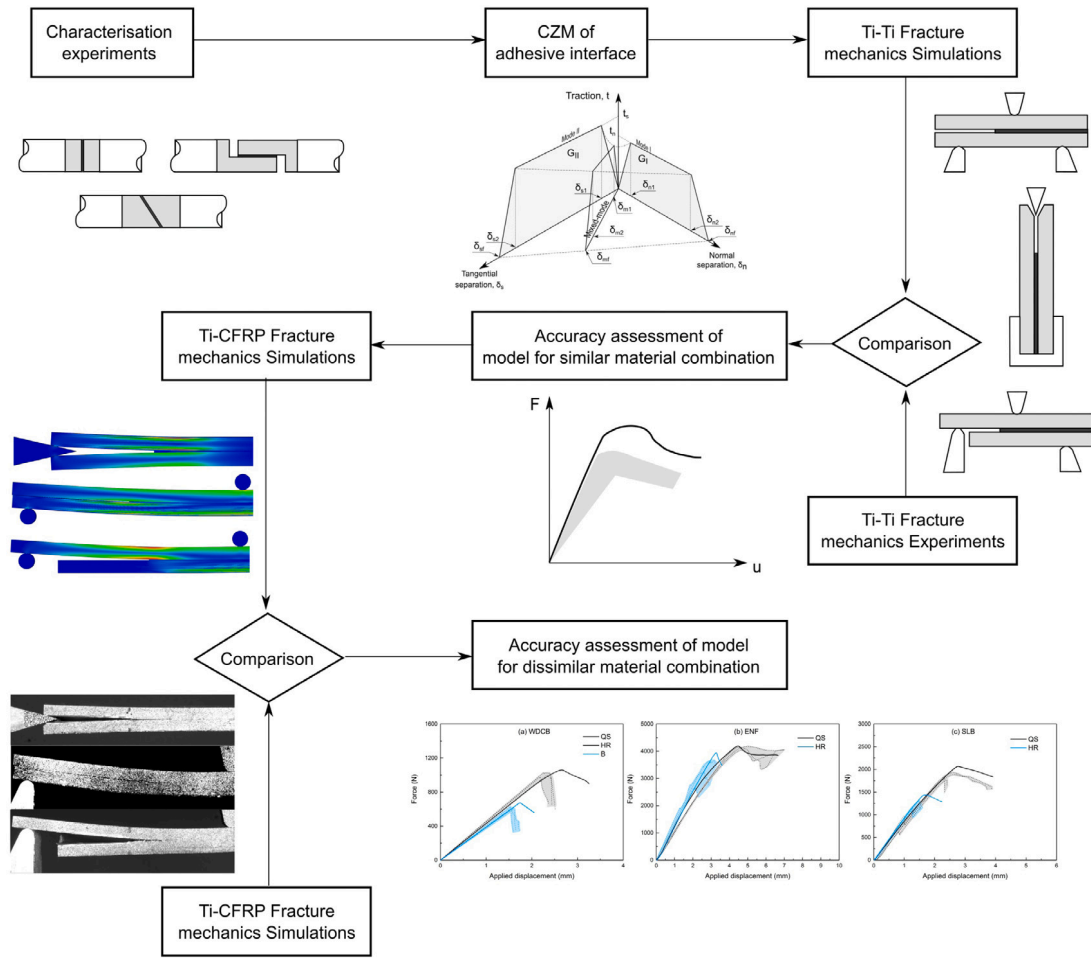
Fig. 14. Overview of the numerical method for predicting the failure performance of multi-material material combinations.

4.1. Adhesive material model: CZM

The CZM for the considered adhesive is summarised in Tables 5 and 6. The rate-dependent formulations for the strength, the dissipated energy and the plateau ratio are represented by Table 5. Since the adhesive tends to exhibit a relatively large volume fraction of voids, the model includes its influence by introducing the following relationship:

$$f_v(t_a) = f_{vref} t_a^{-f_{v0}} \tag{9}$$

where f_{vref} is the reference value and f_{v0} is the thickness sensitivity parameter. The volume fraction of voids affects both the maximum traction and the dissipated energy.

The traction separation law which describes the CZM shows a trapezoidal shape. Its mathematical description and its relevant shape parameters are presented in Table 6. The CZM is graphically illustrated in Fig. 15. Finally, the material parameters of the AF 163-2OST adhesive are summarised in Table 7

4.2. Numerical setup: finite element analysis

For the simulation of the fracture mechanics experiments, finite element analysis (FEA) was employed. The FEA solver Abaqus/Standard was used to perform the simulations. The adherents were discretised using C3D8 elements, while 3D cohesive elements with 4 integration points were used to model the adhesive layer. The numerical model of each specimen configuration follows the same dimensions and boundary conditions used in the experiments as it is shown in Fig. 16. The
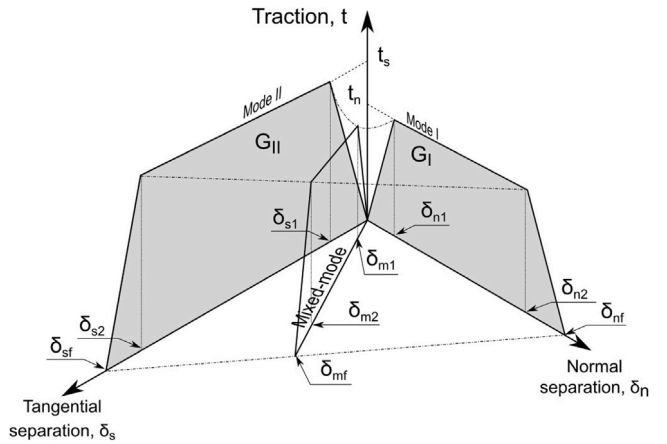

Fig. 15. Graphical illustration of the shape given parameters for the traction separation law (TSL).

size of the mesh was 0.125 x 0.5 x 0.5 mm for the adherent elements and 0.25 x 0.5 x 0.5 mm for the adhesive elements for thickness, width and depth respectively.

The titanium alloy adherents were modelled using an isotropic linear elastic material model using the properties presented in Table 1. For the CFRP adherent, an orthotropic linear elastic material model has been defined using the engineering constants presented in Table 2. The obtained stress values for the composites have been evaluated with

Table 5
Overview of adhesive material model developed and calibrated in [33].

Mode I	
Strength, T	$T_N(\dot{\varepsilon}_N, f_v) = \left[T_{\text{refN}} + T_{0N} \ln\left(\frac{\dot{\varepsilon}_N}{\dot{\varepsilon}_{\text{ref}}}\right) \right](1 - f_v)$
Dissipated energy, G_c	$G_{cN}(\dot{\varepsilon}_N, f_v) = \left[G_{\text{refN}} - G_{0N} \ln\left(\frac{\dot{\varepsilon}_N}{\dot{\varepsilon}_{\text{ref}}}\right) \right](1 - f_v)(1 - \frac{t_0}{t_a})$
Plateau ratio, P	$P_N(\dot{\varepsilon}_N) = P_{\text{refN}} \left(\frac{\dot{\varepsilon}_N}{\dot{\varepsilon}_{\text{ref}}}\right)^{P_N}$
Mode II	
Strength, T	$T_S(\dot{\varepsilon}_S, f_v) = \left[T_{\text{refS}} + T_{0S} \ln\left(\frac{\dot{\varepsilon}_S}{\dot{\varepsilon}_{\text{ref}}}\right) \right](1 - f_v)$
Dissipated energy, G_c	$G_{cS}(\dot{\varepsilon}_S, f_v) = \left[G_{\text{refS}} - G_{0S} \ln\left(\frac{\dot{\varepsilon}_S}{\dot{\varepsilon}_{\text{ref}}}\right) \right](1 - f_v)(1 - \frac{t_0}{t_a})$
Plateau ratio, P	$P_S(\dot{\varepsilon}_S) = P_{\text{refS}} \left(\frac{\dot{\varepsilon}_S}{\dot{\varepsilon}_{\text{ref}}}\right)^{P_S}$

Fig. 16. Representation of boundary conditions (BC) and mesh design for the different experiments.

the Puck IFF criteria for matrix failure. The composite laminate was modelled using one solid C3D8 element per ply through the thickness and the same ply layup as described in Section 2.2. The adhesive layer has been modelled using the material model developed and validated in Lißner et al. [33]. Tables 5 and 6 summarise the adhesive layer model, while Table 7 presents the used material model properties calibrated in Lißner et al. [33,34].

To imitate the experimental boundary conditions, the end of the WDCB specimen is restricted in all the degrees of freedom (DOF). A friction coefficient of 0.1 between the wedge and the specimen arms was chosen. This was verified by comparing the experimental and numerically obtained wedge force–displacement behaviour. Additionally, the movement of the lower supports for ENF and SLB specimens was restricted in all DOF. The loading pin was restricted in all DOF except for displacement in the direction of travel. The same velocity employed in the fracture mechanics experimental setup was applied at the corresponding loading pin.

4.3. Discussion of numerical results

The results of the numerical investigation in QS and HR loading regimes are presented in Fig. 17 for the three different deformation modes. The numerical results for the QS and HR loading regimes show a good agreement with the experiments. It is believed that the simulations of the experiments would provide a more detailed understanding of the failure sequence if one introduces (i) a rate-dependent damage criteria in the CFRP, (ii) cohesive elements or other methods to model delamination or (iii) non-linear shear behaviour [48–51]. Nevertheless, the simulations are in good agreement with the experimental observations.

To understand the individual contribution of each material individually (adhesive and CFRP), the experimental rate-dependent failure envelope presented in Fig. 12 is compared against modelled results. Figs. 18–20 compare the stress histories of both adhesive and CFRP most critical element combinations with their respective failure envelopes for the WDCB, ENF, and SLB experiments. Additionally, the failure criteria for these critical elements are calculated using Eq. (7) for the CFRP and Eq. (8) for the adhesive. The simulations corroborate the experimental observations: CFRP and adhesive layer demonstrate a similar failure performance when loaded in HR and in mode-I dominated environments.

Numerical results for QS WDCB experiments are presented in Fig. 18. One can see that the adhesive layer reached its limit to failure while the CFRP is still at approximately 50% of its full mechanical

Table 6
Overview of the traction separation law shape.

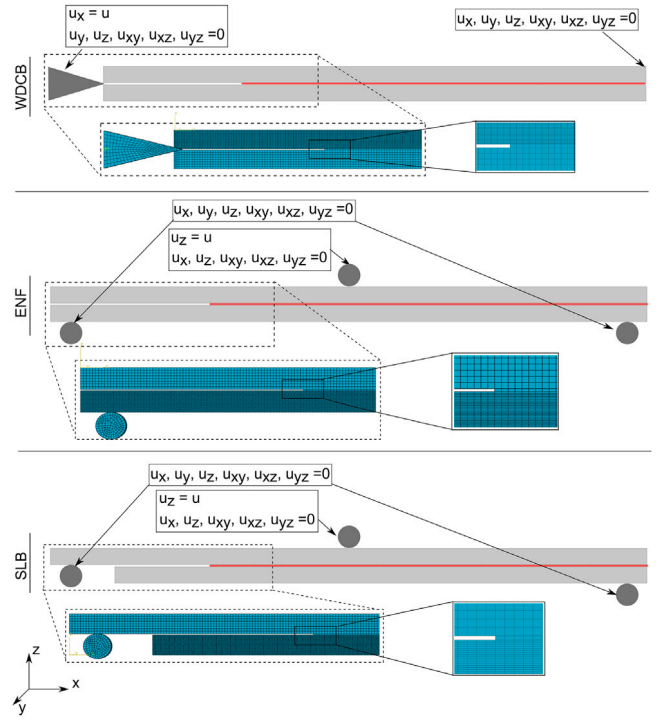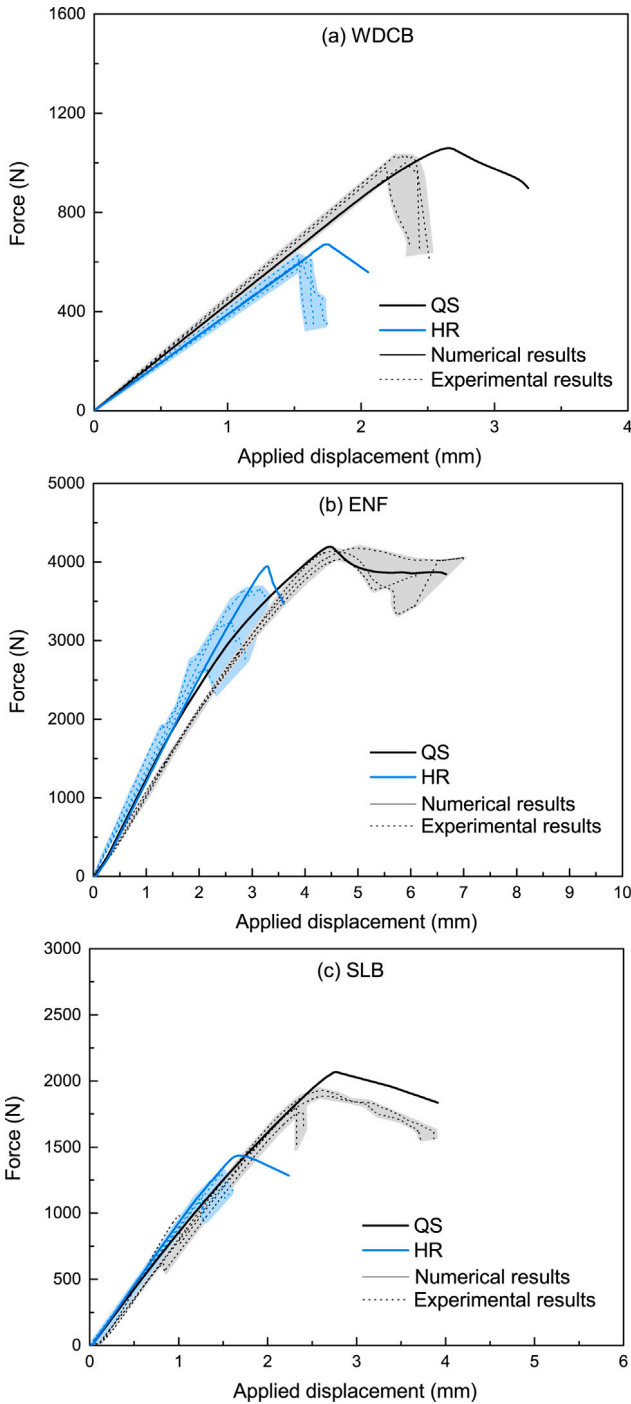| Parameter	Yield initiation, δ_{m1}	Damage initiation, δ_{m2}	Final failure, δ_{mf}
Relationship	$t = (1 - d)K\delta$		
Criterion	$\left(\frac{\delta_{m1,I}}{\delta_{n1}}\right)^2 + \left(\frac{\delta_{m1,II}}{\delta_{s1}}\right)^2 = 1$	$\left(\frac{\delta_{mi,I}}{\delta_{ni}}\right) + \left(\frac{\delta_{mi,II}}{\delta_{si}}\right) = 1, \quad i = 2, f$	
Displacement, δ_m	$\delta_{m1} = \delta_{n1}\delta_{s1}\sqrt{\frac{1+\beta^2}{\delta_{s1}^2 + (\delta_{n1}\beta)^2}}$	$\delta_{mi} = \delta_{ni}\delta_{si}\frac{\sqrt{1+\beta^2}}{(\beta\delta_{ni} + \delta_{si})} \quad i = 2, f$	
Displacements, δ_n, δ_s	$\delta_{n1} = \frac{T_N}{K_n}$ with $K_n = \frac{E}{t_{el}}$	$\delta_{n2} = \delta_{n1} + \frac{2G_{cN}P_N}{T_N(1+\gamma_N)}$	$\delta_{nf} = \delta_{n1} + \delta_{n2} + \frac{2G_{cN}}{T_N\gamma_N} - \frac{\delta_{n2} + \gamma_N(\delta_{n2} - \delta_{n1})}{\gamma_N}$
	$\delta_{s1} = \frac{T_S}{K_s}$ with $K_s = \frac{G}{t_{el}}$	$\delta_{s2} = \delta_{s1} + \frac{2G_{cS}P_N}{T_S(1+\gamma_S)}$	$\delta_{sf} = \delta_{s1} + \delta_{s2} + \frac{2G_{cS}}{T_S\gamma_S} - \frac{\delta_{s2} + \gamma_S(\delta_{s2} - \delta_{s1})}{\gamma_S}$
Equivalent δ_{m1} displacement with mixed-mode ratio	$\delta_{m1} = \sqrt{\delta_{m1,I}^2 + \delta_{m1,II}^2}$ with $\beta = \frac{\delta_{m1,II}}{\delta_{m1,I}}$		
Damage variable	$d = \begin{cases} 0 & , \delta \leq \delta_{m1} \\ 1 - \frac{\delta_{m1}}{\delta} \cdot \left[1 + \frac{(\gamma_m - 1)(\delta - \delta_{m1})}{(\delta_{m2} - \delta_{m1})}\right] & , \delta_{m1} < \delta \leq \delta_{m2} \\ 1 - \left[\frac{\gamma_m \cdot \delta_{m1}}{\delta} \cdot \frac{(\delta_{mf} - \delta)}{(\delta_{mf} - \delta_{m2})}\right] \cdot \left[2 \cdot \left(\frac{\delta - \delta_{m2}}{\delta_{mf} - \delta_{m2}}\right)^3 - 3 \cdot \left(\frac{\delta - \delta_{m2}}{\delta_{mf} - \delta_{m2}}\right)^2 + 1\right] & , \delta_{m2} < \delta \leq \delta_{mf} \\ 1 & , \delta > \delta_f \end{cases}$		
Mixed-mode plateau	$\gamma_m = \sqrt{\frac{\gamma_N^2 + (\beta\gamma_S)^2}{(1+\beta^2)}}$		
Mixed-mode stiffness	$K = \sqrt{\frac{K_n^2 + (\beta K_s)^2}{(1+\beta^2)}}$		

Fig. 17. Numerical results for the investigated fracture modes (a) WDCB, (b) ENF and (c) SLB.

predicted adhesive stresses reached their corresponding failure limit before the CFRP — which is still well within its mechanical capacity for QS and HR loading regimes. Consequently, the failure of the adhesive layer is numerically confirmed. This is in agreement with the fracture observations reported here.

Analogously, Fig. 20 presents the predicted stresses of adhesive and CFRP in SLB simulations. The SLB specimens shows similar behaviour to the WDCB specimens: (i) in QS, the adhesive approached its limit significantly before the CFRP, (ii) in HR, both the CFRP and the adhesive reached their corresponding failure limits at similar times — the stress difference for failure of adhesive and CFRP is relatively small (approximately 10 MPa). Hence, the failure can occur in both materials. This agrees with the experimental observations which revealed full CFRP delamination under HR loading — see Fig. 11.

Numerical simulations of the multi-material adhesive joint structures showed a good reproduction of the experimentally obtained results for different fracture modes and loading rates. The simulations provided clarification on the failure sequence which was observed through the fracture mechanics experiments and analysed *via* high-resolution fractography. This proves the validity of the developed experimental and numerical framework for measuring the most critical quantities related to the fracture of multi-material adhesively bonded structures.

5. Conclusions

The rate-dependent failure performance of multi-material adhesive joints – a combination of CFRP and Ti-6Al-4V adherents – in the form of fracture mechanics experiments (WDCB, ENF and SLB specimens) was investigated. Simulations of the performed experiments were carried out to assess the ability of a CZM for the adhesive layer to predict the experimental observed phenomena. The following conclusions can be drawn:

1. Experimental observations of the investigated fracture modes show a decrease of fracture energy with increasing loading rate. Additionally, under QS conditions, experiments exhibit failure of the adhesive layer. Under HR condition, only the ENF specimens exhibit failure of the adhesive layer while the WDCB and SLB specimens exhibited CFRP damage.
2. Fracture analysis confirms cohesive failure of the adhesive layer independently of fracture modes in QS and ENF mode under HR. HR WDCB exhibits a fracture transition from adhesive layer damage to CFRP damage while HR SLB experiments exhibit exclusively CFRP delamination.
3. The behaviour of the CFRP-Ti multi-material combination is compared to the Ti-Ti combination: the results show similar behaviour independent of adherent material. CFRP-Ti joints exhibit slightly lower maximum forces, slightly higher compliance and similar fracture energy to Ti-Ti joints. The SLB specimens under HR loading condition is the exception: The CFRP-Ti specimen shows significantly lower maximum force and fracture energy due to CFRP failure.
4. The independent fracture properties of each material are used to explain the results. Under QS loading the adhesive exhibits significantly lower stress than CFRP — thus failure of the adhesive layer in fracture mechanics experiments occurs. Under
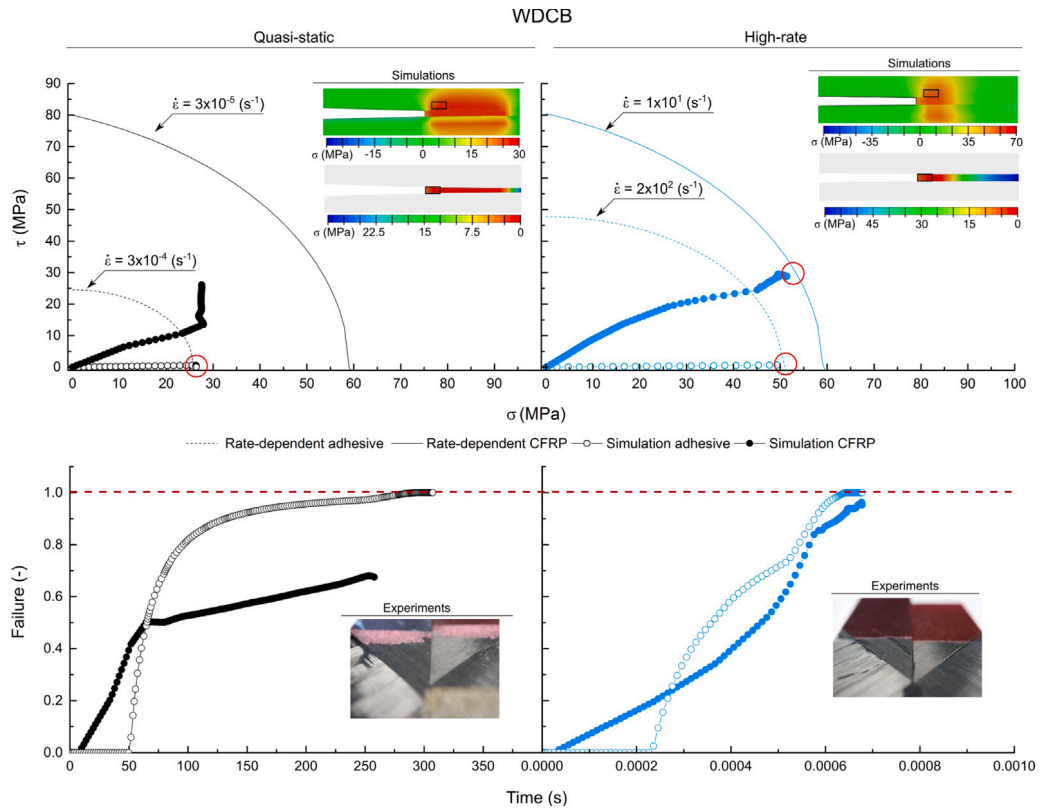
capacity. This is supported by the experimental observations — where the failure of the adhesive layer was evident as seen in the fracture surface micrograph shown in Fig. 9. On the other hand, numerical HR results demonstrate the similar mechanical performance of CFRP and adhesive: stresses of both materials are much closer to their respective failure limits. Considering the relatively small difference in stress (5 MPa) and the inhomogeneous nature of the materials, it is likely that the failure sequence is transferred from the adhesive to the CFRP — as shown in Fig. 9.

Fig. 19 shows the predicted stresses for ENF simulations as a function of material type and loading rate. In both loading regimes the

Fig. 18. Representation of the rate-dependent performance of experimental and numerical observations of adhesive and CFRP for WDCB.
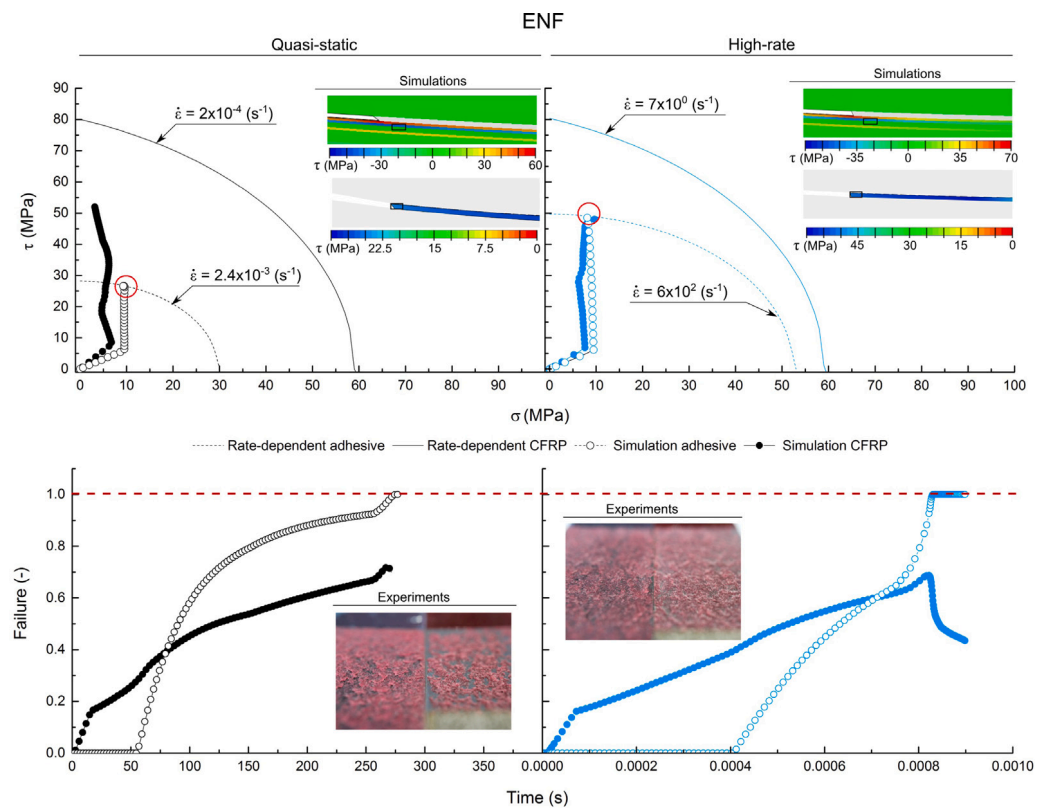

Fig. 19. Representation of the rate-dependent performance of experimental and numerical observations of adhesive and CFRP for ENF.
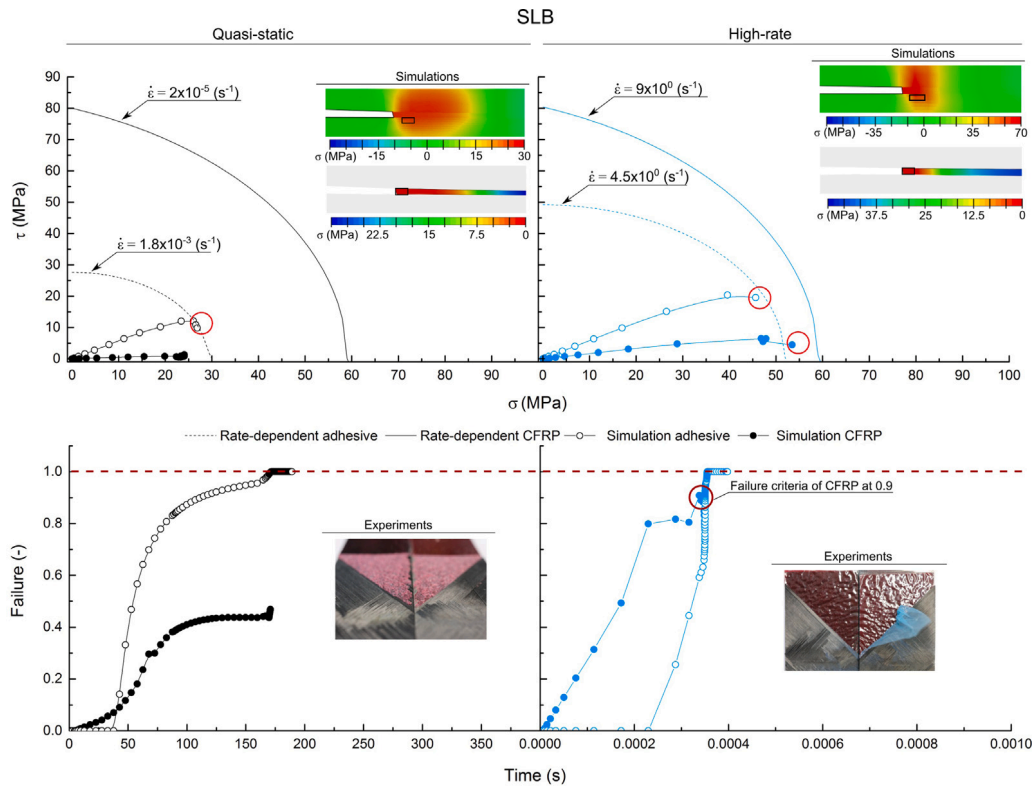
Fig. 20. Representation of the rate-dependent performance of experimental and numerical observations of adhesive and CFRP for SLB experiments.

HR loading the maximum stresses in the adhesive and CFRP are similar, thus the increased chances of CFRP dominated fracture under certain fracture modes.

5. Numerical simulations of the fracture mechanics experiments – which include material models for both adhesive and adherents – are able to accurately predict the observed behaviour as a function of the fracture mode and the loading rate. Hence, the material model of the adhesive has been constitutively validated.

6. Local stresses extracted from the simulations around the most critical locations (adhesive and CFRP interface) are compared to the failure envelope of both adhesive and CFRP. The analysis supports the experimental observations and rationalises the shift from adhesive-controlled failure under QS to CFRP-controlled damage under HR conditions.

7. The numerical analysis emphasises the importance of rate-dependent models for both the adhesive and the CFRP in order to capture the observed experimental findings.

authorship contribution statement

M. Lißner: Conceptualization, Methodology, Formal analysis, Software, Writing - original draft, Visualization, Investigation, Validation. **B. Erice:** Conceptualization, Methodology, Software, Investigation, Validation, Writing - review & editing. **E. Alabort:** Conceptualization, Methodology, Writing - review & editing. **D. Thomson:** Validation, Writing - review & editing. **H. Cui:** Validation, Writing - review & editing. **C. Kaboglu:** Resources. **B.R.K. Blackman:** Resources, Validation, Writing - review & editing. **M. Gude:** Resources. **N. Petrinic:** Supervision.

References

[1] Braga Daniel FO, Tavares SMO, Da Silva Lucas FM, Moreira PMGP, De Castro Paulo MST. Advanced design for lightweight structures: Review and prospects. In: Progress in aerospace sciences. 2014.

[2] Schweizer Nicole, Giessl Andreas, Schwarzhaupt Oliver. Lightweight CFRP wheel w ith electric motor. Auto Tech Rev 2012;1(7):44–7.

[3] Banea MD, Da Silva LFM. Adhesively bonded joints in composite materials: An overview. Proc Inst Mech Eng L 2009;223(1):1–18.

[4] Arouche Marcio Moreira, Wang Wandong, Teixeira de Freitas Sofia, de Barros Silvio. Strain-based methodology for mixed-mode I+II fracture: A new partitioning method for bi-material adhesively bonded joints. J Adhesion 2019;95(5–7):385–404.

[5] Bang CS, Kim JG, Lee DG. Fracture toughness enhancement with reinforcing fibers for adhesively bonded joints under repeated thermal shocks. In: 18th International conference on composite materials; 2011. p. 1–6.

[6] Jiang Zhengwen, Wan Shui, Wu Zhishen. CAlculation of energy release rate for adhesive composite/metal joints under mode-I loading considering effect of the non-uniformity. Composites B 2016;95:374–85.

[7] Di Bella G, Galtieri G, Pollicino E, Borsellino C. Mechanical characterization of adhesive joints with dissimilar substrates for marine applications. Int J Adhesion Adhesives 2013;41:33–40.

[8] Pinto AMG, Magalhães AG, Campilho RDSG, de Moura MFSF, Baptista APM. Single-lap joints of similar and dissimilar adherends bonded with an acrylic adhesive. J Adhesion 2009;85(6):351–76.

[9] Al-Zubaidy Haider, Al-Mahaidi Riadh, Zhao Xiao Ling. Experimental investigation of bond characteristics between CFRP fabrics and steel plate joints under impact tensile loads. Compos Struct 2012;94(2):510–8.

[10] Wang Wandong, Lopes Fernandes Romina, Teixeira De Freitas Sofia, Zarouchas Dimitrios, Benedictus Rinze. How pure mode I can be obtained in bi-material bonded DCB joints: A longitudinal strain-based criterion. Composites B 2018;153(March):137–48.

[11] Marannano G, Zuccarello B. Static strength and fatigue life of optimized hybrid single lap aluminum–CFRP structural joints. J Adhesion 2018;94(7):501–28.

[12] Rudawska Anna. Adhesive joint strength of hybrid assemblies: Titanium sheet-composites and aluminium sheet-compositesexperimental and numerical verification. Int J Adhesion Adhesives 2010;30(7):574–82.

[13] Afendi Mohd, Teramoto Tokuo, Bakri Hairul Bin. Strength prediction of epoxy adhesively bonded scarf joints of dissimilar adherends. Int J Adhesion Adhesives 2011;31(6):402–11.

[14] Teixeira de Freitas Sofia, Sinke Jos. Failure analysis of adhesively-bonded metal-skin-to-composite-stiffener: Effect of temperature and cyclic loading. Compos Struct 2017;166:27–37.

[15] Teixeira de Freitas Sofia, Sinke Jos. Failure analysis of adhesively-bonded skin-to-stiffener joints: Metal-metal vs. composite-metal. Eng Fail Anal 2015;56:2–13.

[16] Saleh Mohamed Nasr, Saeedifar Milad, Zarouchas Dimitrios, De Freitas Sofia Teixeira. Stress analysis of double-lap bi-material joints bonded with thick adhesive. Int J Adhesion Adhesives 2020;97(November 2019):102480.

[17] Alía Cristina, Arenas José M, Suárez Juan C, Ocaña Rosa, Narbón Julián J. Mode II fracture energy in the adhesive bonding of dissimilar substrates: Carbon fibre composite to aluminium joints. J Adhes Sci Technol 2013;27(22):2480–94.

[18] Qiao Pizhong, Chen Fangliang, Hamey Cole S, Wang Jialai. Mixed-mode fracture of hybrid material bonded interfaces under four-point bending. J Aerosp Eng 2009;24(2):218–26.

[19] Ouyang Zhenyu, Li Guoqiang. Nonlinear interface shear fracture of end notched flexure specimens. Int J Solids Struct 2009;46(13):2659–68.

[20] Ouyang Zhenyu, Ji Gefu, Li Guoqiang. On approximately realizing and characterizing pure mode-I interface fracture between bonded dissimilar materials. J Appl Mech 2011;78(3):1–11.

[21] Arenas José M, Ocaña Rosa, Alía Cristina, Narbón Julián J, Islán Manuel. Fracture energy in structural adhesive joints of composite-aluminum under adverse environments conditions. J Adhes Sci Technol 2014;28(2):201–14.

[22] Boeman Raymond G, Erdman DL, Klett LB, Lomax RD. A practical test method for mode I fracture toughness of adhesive joints with dissimilar substrates. In: SAMPE-ACCE-DOE advanced composites conference; 1999. p. 1–9.

[23] Khoshravan Mohammadreza, Asgari Mehrabadi Farhad. Fracture analysis in adhesive composite material/aluminum joints under mode-I loading; experimental and numerical approaches. Int J Adhesion Adhesives 2012;39:8–14.

[24] Tsokanas P, Loutas T, Kostopoulos V, Essa Y, Martin de la Escalera F. On the design and analysis of interlaminar fracture toughness tests on dissimilar metal-composite adhesive joints with residual thermal stresses. In: ECCM 18 - 18th European Conference on Composite Materials, Athens, Greece, 24–28th June 2018.

[25] Anyfantis Konstantinos N. Finite element predictions of composite-to-metal bonded joints with ductile adhesive materials. Compos Struct 2012;94(8):2632–9.

[26] Galvez Pedro, Quesada Alejandro, Martinez Miguel Angel, Abenojar Juana, Boada Maria Jesus L, Diaz Vicente. Study of the behaviour of adhesive joints of steel with CFRP for its application in bus structures. Composites B 2017;129:41–6.

[27] Machado JJM, Marques EAS, da Silva LFM. Adhesives and adhesive joints under impact loadings: An overview. J Adhes 2018;94(6):421–52.

[28] Al-Mosawe Alaa, Al-Mahaidi Riadh. Effect of impact ?lload on the bond between steel and CFRP laminate. Int J Chem Mol Nucl Mater Metall Eng 2015;9(1):84–7.

[29] Avendaño R, Carbas RJC, Chaves FJP, Costa M, da Silva LFM, Fernandes AA. Impact loading of single lap joints of dissimilar lightweight adherends bonded with a crash-resistant epoxy adhesive. J Eng Mater Technol 2016;138(4):1–10.

[30] Zhao Xiao-Ling, Bai Yu, Al-Mahaidi Riadh, Rizkalla Sami. Effect of dynamic loading and environmental conditions on the bond between CFRP and steel: State-of-the-art review. J Compos Construct 2013;18(3):A4013005.

[31] Marzi Stephan, Biel Anders, Stigh Ulf. On experimental methods to investigate the effect of layer thickness on the fracture behavior of adhesively bonded joints. Int J Adhesion Adhesives 2011;31(8):840–50.

[32] Kadioglu Ferhat, Adams Robert D. Flexible adhesives for automotive application under impact loading. Int J Adhesion Adhesives 2015;56:73–8.

[33] Lißner M, Alabort E, Cui H, Rito R, Blackman B RK, Petrinic N. Experimental characterisation and numerical modelling of the influence of bondline thickness, loading rate, and deformation mode on the response of ductile adhesive interfaces. J Mech Phys Solids 2019;130:349–69.

[34] Lißner Maria, Alabort Enrique, Erice Borja, Cui Hao, Blackman Bamber R K, Petrinic Nik. On the dynamic response of adhesively bonded structures. Int J Impact Eng 2020;138(June 2019):103479.

[35] Yamagata Yuki, Lu Xi, Sekiguchi Yu, Sato Chiaki. Experimental investigation of mode I fracture energy of adhesively bonded joints under impact loading conditions. Appl Adhesion Sci 2017;5(7):1–10.

[36] Li S, Thouless MD, Waas AM, Schroeder JA, Zavattieri PD. Mixed-mode cohesive-zone models for fracture of an adhesively bonded polymer-matrix composite. Eng Fract Mech 2006;73(1):64–78.

[37] Blackman BRK, Kinloch AJ, Paraschi M. The determination of the mode II adhesive fracture resistance, GIIC, of structural adhesive joints: An effective crack length approach. Eng Fract Mech 2005;72:877–97.

[38] Melcher RJ, Johnson WS. Mode I fracture toughness of an adhesively bonded composite-composite joint in a cryogenic environment. Compos Sci Technol 2007;67(3–4):501–6.

[39] Jacob George C, Starbuck J Michael, Fellers John F, Simunovic Srdan, Boeman Raymond G. The effect of loading rate on the fracture toughness of fiber reinforced polymer composites. J Appl Polym Sci 2005;96(3):899–904.

[40] Hoffmann Justus. An investigation into the characterisation and modelling of the impact response of CFRP [Ph.D. thesis], University of Oxford; 2018.

[41] Ashby Michael. Materials selection in mechanical design: Fourth edition. Mater Sel Mech Design: Fourth Ed. 2010;9780080952:1–646.

[42] Alvarez Feito Diego. Fracture mechanics of carbon fibre reinforced plastics to Ti-alloy adhesive joints [Ph.D. thesis], Imperial College London; 2012.

[43] de Moura MFSF, Silva MAL, de Morais AB, Morais JJL. Equivalent crack based mode II fracture characterization of wood. Eng Fract Mech 2006;73(8):978–93.

[44] Oliveira Jorge MQ, De Moura Marcelo FSF, Morais José JL. Application of the end loaded split and single-leg bending tests to the mixed-mode fracture characterization of wood. Holzforschung 2009;63(5):597–602.

[45] Cui Hao. Delamination and debonding failure of laminated composite T-joints [Ph.D. thesis], TU Delft; 2014.

[46] Blackman BRK, Kinloch AJ, Rodriguez-Sanchez FS, Teo WS. The fracture behaviour of adhesively-bonded composite joints: Effects of rate of test and mode of loading. Int J Solids Struct 2012;49(13):1434–52.

[47] Puck A, Schürmann H. Failure analysis of FRP laminates by means of physically based phenomenological models. Compos Sci Technol 1998;58(7):1045–67.

[48] Thomson Daniel M, Erice Borja, Cui Hao, Hoffmann Justus, Wiegand Jens, Petrinic Nik. A puck-based localisation plane theory for rate- and pressure-dependent constitutive modelling of unidirectional fibre-reinforced polymers. Compos Struct 2018;184(September 2017):299–305.

[49] Sun CT, Chen JL. A simple flow rule for characterizing nonlinear behavior of fiber composites. J Compos Mater 1989;23(10):1009–20.

[50] Vogler M, Rolfes R, Camanho PP. Modeling the inelastic deformation and fracture of polymer composites-Part I: Plasticity model. Mech Mater 2013;59:50–64.

[51] Vyas GM, Pinho ST, Robinson P. Constitutive modelling of fibre-reinforced composites with unidirectional plies using a plasticity-based approach. Compos Sci Technol 2011;71(8):1068–74.